JOURNAL OF AIRCRAFT
Vol. 42, No. 4, July–August 2005

Modeling of Aerodynamic Coupling Between Aircraft in Close Proximity

Atilla Dogan* and Sriram Venkataramanan†
University of Texas at Arlington, Arlington, Texas 76019
and
William Blake‡
U.S. Air Force Research Laboratory, Wright–Patterson Air Force Base, Ohio 45433

A method is developed for modeling the aerodynamic coupling between aircraft flying in close proximity. Velocities induced on a trailing aircraft by vortices from an aircraft upstream are written as a function of the relative separation and relative orientation between the two aircraft. The nonuniform vortex-induced wind and wind gradients acting on the trail aircraft are approximated as effective uniform wind and wind gradients. In a dynamic simulation, the effective wind can be used directly in the equations of motion, whereas the wind gradient can be used in the standard buildup equations for the aerodynamic moments. This removes necessity to explicitly compute the induced forces and moments. Various vortex models for estimating induced velocities and averaging schemes for computing effective wind components and gradients are assessed. Results from the method are compared to wind-tunnel data for a formation of two similar aircraft. A good match is obtained between experimental data and the predicted incremental force and moment coefficients induced on the trail aircraft. It is briefly discussed how the effective wind components and gradients can be incorporated into equations of motion of aircraft flying in a vortex field.

Nomenclature

a = coordinate along wing axis, m; position of point P relative to wing aerocenter
$[\hat{\underline{B}}]$ = vectrix of body frame
b = wing span, m
b' = effective wing span, m
$\bar{c}$ = wing mean chord, m
D_F = diameter of the fuselage, m
$f_{(.)(*)}$ = weighting function of $W_{(.)}$ used for averaging along the body $(*)$ direction
$I_{m \times m}$ = identity matrix of order m
L_F = length of the fuselage, m
P = arbitrary point moved along the body dimensions of ith unmanned aerial vehicle (UAV)
p = position of point P with respect to the virtual-leader (VL) frame; component of angular velocity around body x axis, rad/s
q = component of angular velocity around body y axis, rad/s
R = position of point P relative to the effective wing tip, m
$\boldsymbol{R}_{(.)(*)}$ = rotation matrix from frame $(*)$ to frame (.)
r = radial distance of point P to vortex filament, m; component of angular velocity around body z axis, rad/s
r_c = radius of vortex core, m
$\mathcal{S}$ = wing area, m
V = effective air velocity, m/s
V_{wt} = wind-tunnel test velocity, m/s
$[\hat{\underline{VL}}]$ = vectrix of virtual-leader frame
υ_P = position of point P with respect to the center of mass, m
$\upsilon_{\mathrm{R,L}}$ = position of the effective right and left wing tips relative to the c.m., m
W_{Bi} = representation of induced velocity vector written in the body frame of ith UAV
$W_{i_{\mathrm{R,L}}}$ = tangential wind velocity induced at point P by the right and left filaments, m/s
$W_{\mathrm{SW}_{i_{\mathrm{R,L}}}}$ = component of $W_{i_{\mathrm{R,L}}}$ in the y direction of the wind frame of kth UAV, m/s
$W_{\mathrm{UW}_{i_{\mathrm{R,L}}}}$ = component of $W_{i_{\mathrm{R,L}}}$ in the negative z direction of the wind frame of kth UAV, m/s
W_{wk} = representation of induced velocity vector written in the wind frame of kth UAV
$W_{x,y,z}$ = components of W_{Bi} in the x, y, z directions
$\tilde{W}_{(.)1(*)}$ = average of (.) component of W_{Bi} from the lower limit to zero in the body $(*)$ direction
$\tilde{W}_{(.)2(*)}$ = average of (.) component of W_{Bi} from zero to the upper limit in the body $(*)$ direction
$[\hat{\underline{w}}]$ = vectrix of wind frame
x, y, z = components of ξ in x, y, z directions, m
x_0, z_0 = coordinates of the aerodynamic center in x, z directions of body frame, m
α = effective angle of attack, deg or rad
β = effective sideslip angle, deg or rad
Γ = vortex strength, m
γ = representation of R in the wind frame of kth UAV
ζ = dihedral angle, deg or rad
$\theta_{\mathrm{R,L}}$ = angle between $W_{i_{\mathrm{R,L}}}$ and y axis of the wind frame of kth UAV, deg or rad
Λ = sweepback angle at quarter-chord, deg or rad
ν = fluid viscosity, m^2/s
ξ = position of center of mass relative to VL frame
ρ = position of the effective wing tip relative to the VL frame
τ = age of the vortex, s
(.) = representation of the vector quantity $\underline{(.)}$ in the frame in which it is originally defined

---

Presented as Paper 2003-5385 at the AIAA Atmospheric Flight Mechanics Conference, Austin, TX, 11–14 August 2003; received 3 March 2004; revision received 21 September 2004; accepted for publication 22 September 2004.

*Assistant Professor, Department of Mechanical and Aerospace Engineering. Member AIAA.

†Graduate Student, Department of Mechanical and Aerospace Engineering. Student Member AIAA.

‡Aerospace Engineer. Associate Fellow AIAA.

$\underline{(.)}$ = vector quantity

Subscripts

B = body frame
eff = effective wind quantities on ith UAV
I = inertial frame
i = ith UAV (vortex-encountering UAV)
k = kth UAV (vortex-generating UAV)
net = combined effect of left and right filaments
R, L = right and left vortex filaments respectively of kth UAV
VL = virtual-leader frame
w = wind frame
x, y, z = components of a vector in the x, y, z axes

Superscripts

T = matrix/vectrix transpose
$\sim$ = averaged wind on ith UAV

I. Introduction

THE trailing vortex field generated by an aircraft in flight can significantly affect the dynamics of other aircraft flying closely behind it. The effect of such aerodynamic coupling has been viewed as a mixed blessing in the aerospace community. Although the effect of the leader's vortices on the follower in a formation flight is beneficial in reducing drag/fuel consumed,[1] the influence of a tanker's vortices on a receiver aircraft during aerial refueling[2,3] can be detrimental to the stability of the receiver aircraft. Similarly, the effect of wake vortices from the preceding aircraft is a cause for major concern during aircraft takeoff/landing operations. A reasonably accurate model of such aerodynamic coupling is needed to conduct a realistic, nonlinear, six-degree-of-freedom (DOF) simulation study of aircraft flying in close proximity.[4,5]

Previous techniques used to model the vortex-induced effects include averaging the upwash and sidewash,[6] strip theory,[7] and computation of large data sets for table look-up. Although the first two techniques involve calculation of induced angles of attack and sideslip from the wind distribution, which are used to eventually determine the induced forces and moments, the table look-up method requires handling huge amounts of data (usually from a wind/water-tunnel or flight test). Moreover, there have been restrictions on the relative separations and orientations between the lead and trail aircraft for the vortex effect to be determined.

In this work, we develop a new way of implementing the vortex effect in standard dynamic equations of motion and aerodynamic buildup equations with wind-effect terms included.[4,5] The wind-effect terms in these equations are considered to be based on the uniform wind distribution acting at the aircraft's c.m. However, the vortex-induced wind field acting on the encountering aircraft is nonuniform in nature. Therefore, to be able to use the standard equations with wind effect directly there is a need to approximate the nonuniform induced wind components and gradients by equivalent uniform wind and gradients. Once a reasonable approximation is achieved, the implementation of aerodynamic coupling between aircraft flying in close proximity becomes far more direct and computationally efficient than the conventional procedure because the necessity for calculating the induced forces and moments during the simulation is overcome. The need for a simple and fairly accurate method of approximating the nonuniform vortex-induced wind field by its uniform equivalent is the motivation for the material presented in this paper.

The paper is organized as follows. First, the reference frames and the notation considered in modeling the relative position and orientation of multiple aircraft are presented in Sec. II. Next, our novel approach of modeling the aerodynamic coupling is introduced in Sec. III. Then, various vortex models and averaging schemes that could be employed by our technique are described in Secs. IV and V, respectively. In Sec. VI, the comparison and calibration analysis carried out on our vortex-effect modeling technique is discussed. Section VI.A presents an analytical verification for a simple case of relative separation, and Sec. VI.B compares the results of the method against measurements from a wind-tunnel test. Here, results produced by the various vortex models and averaging schemes explained are analyzed, and the vortex model/averaging scheme combination that gives the best match with the experimental data is identified. Finally, Sec. VII discusses how the effective wind components and gradients are incorporated into six-DOF equations of motion of aircraft flying in close proximity.

II. Reference Frames and Notation

In the development of the vortex-effect modeling between aircraft/unmanned aerial vehicles (UAVs) flying in close proximity, there are four basic reference frames involved: 1) inertial frame, 2) virtual-leader (VL) frame, 3) body frame of each UAV, and 4) wind frame of each UAV. The inertial frame is on the ground, and its z axis is pointing downwards. The reason for introducing the VL frame as an intermediate reference frame is as follows. Because one of the applications of our work is the reconfiguration of a UAV formation,[4] a frame fixed to one of the UAVs (either the actual leader or a follower) as the reference frame for the individual UAVs of the formation can lead to a change in the relative positions of all the UAVs if there comes a need to reposition the UAV whose body/wind frame is chosen as the reference. Hence to avoid such a situation, we write the equations of the individual UAVs in the frame of a virtual leader. The VL frame is always aligned with the inertial frame and moves along the desired trajectory of the formation. In other words, the axes of the VL frame are always parallel to those of the inertial frame even if the VL frame has a translational motion relative to the inertial frame (Fig. 1). The body frame and the wind frame of each UAV are attached to and move with the c.m. of the UAV. The orientation of the body frame relative to the inertial frame is expressed in standard 3-2-1 Euler angle notation. For cases involving multiple reference frames, vectrix formalism[8] facilitates an efficient transformation of vectors from one frame to another using rotation matrices. This feature of vectrix formalism enables the vector equations to be converted easily into the corresponding matrix equations, which are more suitable for implementation in a simulation software. The vectrix of a frame is defined to be the array of unit vectors ($\underline{\hat{\imath}}$, $\underline{\hat{\jmath}}$, $\underline{\hat{k}}$) of the frame and is denoted by

$$[\underline{\hat{(.)}}] = \begin{bmatrix} \underline{\hat{\imath}} \\ \underline{\hat{\jmath}}_{(.)} \\ \underline{\hat{k}}_{(.)} \end{bmatrix} \tag{1}$$

Hence, a vector can be written as the product of the transpose of the vectrix of a frame and the representation of the vector in that frame. In this paper, we follow the notation where A is considered to be the representation of a vector $\boldsymbol{A}$ written in the frame in which it is originally defined. All matrices are written in bold font. Figure 2

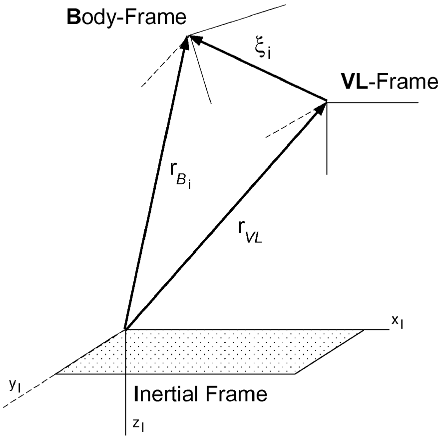

Fig. 1 VL frame used as an intermediate reference frame.

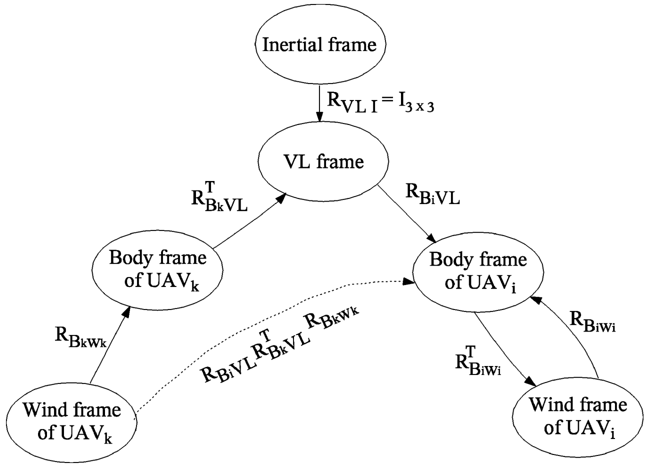

Fig. 2 Various frames and rotation matrices.

shows the various reference frames for a two-UAV (UAV$_i$ and UAV$_k$) group and the rotation matrices used to transform a vector from one frame to another.

Although our aircraft model[4] and the multiaircraft simulation[9] have been primarily developed for the formation flight of UAVs, the model of aerodynamic coupling has been developed in such a way that it could be applied generally to any flight situation, such as aerial refueling or airport/carrier takeoff and landing operations, involving multiple aircraft in close proximity. In the sections to follow, the notation UAV$_k$ is used to denote the vortex-generating UAV (which corresponds to the leader UAV in formation flight, the tanker UAV in aerial refueling and the preceding UAV to have taken-off/landed in takeoff/landing operation), and the notation UAV$_i$ is used to denote the UAV that is subject to the wake vortex generated by UAV$_k$. For example, UAV$_i$ stands for the follower UAV in formation flight, the receiver UAV in aerial refueling, and the UAV following UAV$_k$ in takeoff/landing operation.

III. Methodology

There are two major steps involved in our model of aerodynamic coupling: 1) computation of the vortex-induced wind velocity field and 2) approximation of the nonuniform velocity field by uniform (effective) wind components and gradients.

A. Computation of the Vortex-Induced Wind Velocity

In our multiaircraft model, every UAV (say, UAV$_k$) is considered to produce two straight, semi-infinite trailing vortex filaments that induce additional wind velocities on the body of the encountering UAV (say, UAV$_i$). These vortex-induced wind velocities cause changes in the forces and moments experienced by UAV$_i$. However, instead of attempting to directly estimate the induced forces and moments on UAV$_i$, the induced wind velocity and wind gradient components are computed. The induced wind velocities are written as a function of the relative separation and orientation between UAV$_k$ and UAV$_i$ using a suitable vortex model. Because the induced wind and wind gradients are nonuniform along the body of UAV$_i$, an averaging technique is implemented to compute the effective wind and wind gradient as uniform approximations. The effective wind components and gradients are introduced into the nonlinear aircraft equations that include the components of wind and the temporal variation of wind in the body frame (see Sec. VII) to determine the effect on UAV$_i$'s dynamics. The effect of vortex decay over time is also included in the vortex model. Special care has been taken to accommodate different geometrical dimensions for UAV$_k$ and UAV$_i$ and also to include many useful geometrical parameters of the UAVs such as the wing sweep angle, the dihedral angle, and the relative distance between the center of mass of the UAV and the aerodynamic center of the wing in estimating the vortex effect experienced during close proximate flight.

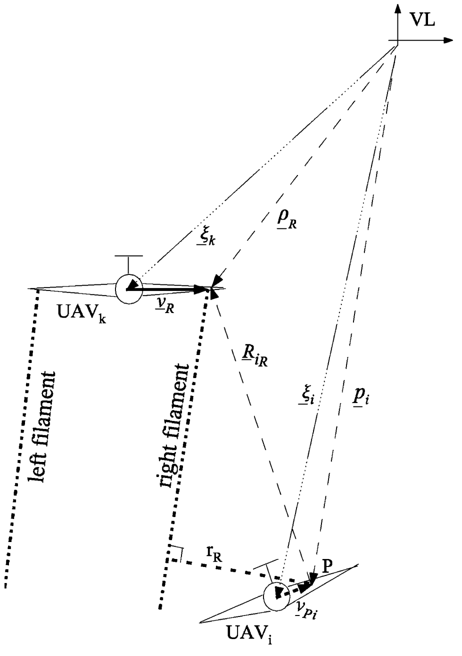

Fig. 3 Vortex model relative to the VL frame.

In this section, we assume that UAV$_i$ is aerodynamically affected by only UAV$_k$. If there is more than one UAV affecting UAV$_i$, then the total induced velocity is considered to be the vectorial sum of the velocities generated by each of the individual vortex-generating UAVs. UAV$_k$ produces two straight, semi-infinite trailing vortex filaments (one each from the right and left wings) that stay parallel to its velocity vector, with the transverse separation equal to the effective wing span b'_k (which is $\pi/4$ times the actual wing span b_k[10]). The induced upwash and sidewash experienced by UAV$_i$ as a result of the trailing vortices from UAV$_k$ are calculated next.

Using a suitable vortex model (see Sec. IV), we obtain the induced velocity vectors $\underline{\boldsymbol{W}}_{i_R}$ and $\underline{\boldsymbol{W}}_{i_L}$ acting at an arbitrary point P on UAV$_i$ by the right and left vortex filaments, respectively. In each vortex model, induced wind vectors at a point are functions of the radial distance of the point to the corresponding vortex filament. Thus, given the relative separation and orientation of the UAVs and their geometric properties (e.g., dihedral angle, sweep angle) we need to find the radial distance of a point on the following UAV to the right and left filament emanating from the vortex-generating UAV.

The right and left filaments are parallel to the velocity vector of UAV$_k$, which is aligned with the x axis of the UAV$_k$'s wind frame. Thus, we need to perform a series of operations on a group of vectors that are shown in Fig. 3 to obtain the radial distances r_R and r_L from point P on the UAV$_i$ to the right and left vortex filaments, respectively.

We first define the position vectors of the c.m. of UAV$_i$ and UAV$_k$ relative to the VL frame to be $\underline{\boldsymbol{\xi}}_i$ and $\underline{\boldsymbol{\xi}}_k$, respectively. Following the notation for the vector and its representation defined earlier in Sec. II, we have

$$\underline{\boldsymbol{\xi}}_i = [\widehat{\underline{VL}}]^T \xi_i \tag{2}$$

where

$$\xi_i = \begin{bmatrix} x_{B_i} \\ y_{B_i} \\ z_{B_i} \end{bmatrix} \tag{3}$$

In Eq. (3), $(x_{B_i}, y_{B_i}, z_{B_i})$ are the separation coordinates of UAV$_i$ from the VL frame expressed in the VL frame. Then, the position vectors of the effective wing tips, which are the origins of the right and left vortex filaments, are defined with respect to the body frame

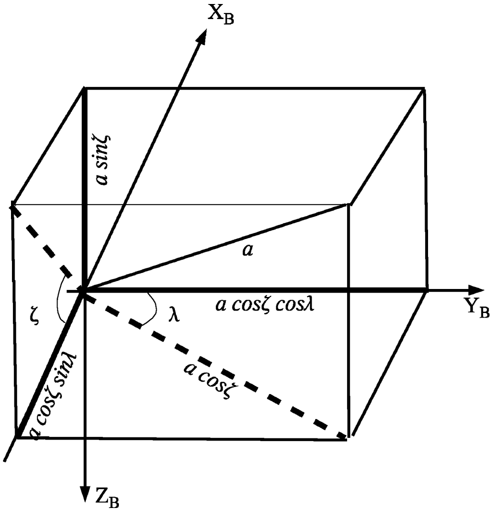

Fig. 4 Wing sweep and dihedral effect.

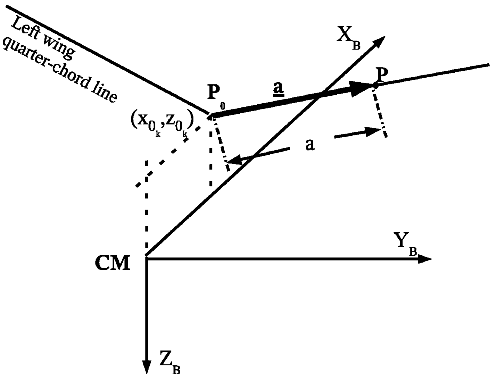

Fig. 5 Separation between c.m. and wing-root quarter-chord.

of UAV$_k$ as $\underline{\boldsymbol{v}}_R$ and $\underline{\boldsymbol{v}}_L$. The geometric parameters of UAV$_k$ like the sweepback angle at quarter-chord Λ_k and dihedral angle ζ_k are taken into consideration through these position vectors. If a is the distance of a point on the wing of UAV$_k$ from its root, then it is evident from Fig. 4 that the vector $\underline{\boldsymbol{a}}$ includes nonzero x and z components as a result of Λ_k and ζ_k. Further, because the relative distance between the c.m. and the wing quarter-chord (generally considered to be the aerodynamic center) of UAV$_k$ given by constants x_{0_k} and z_{0_k} in its body x and z directions (Fig. 5), the position vector $\boldsymbol{v}_R$ is written as

$$\underline{\boldsymbol{v}}_R = [\underline{\hat{B}_k}]^T v_R \tag{4}$$

where

$$v_R = \begin{bmatrix} x_{0_k} - \dfrac{b'_k}{2}\cos\zeta_k \sin\Lambda_k \\[2ex] \dfrac{b'_k}{2}\cos\zeta_k\cos\Lambda_k \\[2ex] z_{0_k} - \dfrac{b'_k}{2}\sin\zeta_k \end{bmatrix} \tag{5}$$

and b'_k denotes the span of UAV$_k$'s effective wing.

Writing this position vector in the VL frame, we get

$$\underline{\boldsymbol{v}}_R = [\underline{\widehat{\text{VL}}}]^T \left(\boldsymbol{R}^T_{B_k\text{VL}}\right) v_R \tag{6}$$

Similarly, the position vector to a point P whose distance from the wing-root quarter-chord is a, on the right or left wing of UAV$_i$, is written in the body frame of UAV$_i$ as

$$\underline{\boldsymbol{v}}_{P_i} = \underline{a}_i + \begin{bmatrix} x_{0_i} \\ 0 \\ z_{0_i} \end{bmatrix} \tag{7}$$

with

$$a_i = \begin{bmatrix} -|a|\cos\zeta_i \sin\Lambda_i \\ a\cos\zeta_i\cos\Lambda_i \\ -|a|\sin\zeta_i \end{bmatrix} \tag{8}$$

where $|a|$ stands for the absolute value of a and positive values of a represent points on the right wing while negative values represent those on the left wing. In the VL frame, the vector $\underline{\boldsymbol{v}}_{P_i}$ is written as

$$\underline{\boldsymbol{v}}_{P_i} = [\underline{\widehat{VL}}]^T \left(\boldsymbol{R}^T_{B_i\text{VL}}\right) v_{P_i} \tag{9}$$

As seen from Fig. 3, the position of the origin of the vortex filament on the right wing of UAV$_k$ relative to the VL frame is the vectorial sum of its position relative to the body frame of UAV$_k$ whose origin is at its c.m. and the position of the c.m. relative to the VL frame. Thus,

$$\underline{\rho}_R = \underline{\boldsymbol{v}}_R + \underline{\boldsymbol{\xi}}_k \tag{10}$$

which from Eq. (6) implies

$$\underline{\rho}_R = [\underline{\widehat{VL}}]^T \left\{\xi_k + \left(\boldsymbol{R}^T_{B_k\text{VL}}\right) v_R\right\} \tag{11}$$

Similarly, we see from Fig. 3 that

$$\underline{\boldsymbol{p}}_i = \underline{\boldsymbol{\xi}}_i + \underline{\boldsymbol{v}}_{P_i} \tag{12}$$

which by virtue of Eqs. (2) and (9) implies

$$\underline{\boldsymbol{p}}_i = [\underline{\widehat{VL}}]^T \left\{\xi_i + \left(\boldsymbol{R}^T_{B_i\text{VL}}\right) v_{P_i}\right\} \tag{13}$$

Further, it can be seen that

$$\underline{\boldsymbol{R}}_{i_R} = \underline{\rho}_R - \underline{\boldsymbol{p}}_i \tag{14}$$

Thus, substituting Eqs. (11) and (13) we get the VL frame representation of the position vector of the point P relative to the UAV$_k$'s effective right wing tip. Thus,

$$R_{i_R} = \xi_k + \left(\boldsymbol{R}^T_{B_k\text{VL}}\right) v_R - \xi_i - \left(\boldsymbol{R}^T_{B_i\text{VL}}\right) v_{P_i} \tag{15}$$

$$\underline{\boldsymbol{R}}_{i_R} = [\underline{\widehat{VL}}]^T R_{i_R} \tag{16}$$

Recall that the vortex filaments are along the velocity vector (x axis of the wind frame), and note that the induced velocity at a point is tangent to a hypothetical circle, which is centered at the intersection point with the filament and on a plane perpendicular to it (Fig. 6). We thus need to transform $\underline{\boldsymbol{R}}_{i_R}$ from the VL frame to the wind frame of UAV$_k$ (w_k) to get the radial distance from the point P on UAV$_i$'s wing to the right filament. We do so by using rotation matrices 1) from VL frame to its body frame (B_k) and 2) from its body frame to its wind frame. Thus,

$$\begin{aligned} \underline{\boldsymbol{R}}_{i_R} &= [\underline{\hat{B}_k}]^T \left(\boldsymbol{R}_{B_k\text{VL}}\right) R_{i_R} \\ &= [\underline{\hat{w}_k}]^T \gamma_R \end{aligned} \tag{17}$$

where $\gamma_R = (\boldsymbol{R}^T_{B_k w_k})(\boldsymbol{R}_{B_k\text{VL}}) R_{i_R}$. Let γ_R be

$$\begin{bmatrix} \gamma_{R_x} \\ \gamma_{R_y} \\ \gamma_{R_z} \end{bmatrix}$$

The radial distance r_R from point P to the right vortex filament is obtained by considering the projection of $\underline{\boldsymbol{R}}_{i_R}$ on the yz plane of the wind frame of UAV$_k$. Thus,

$$r_R = \sqrt{\gamma^2_{R_y} + \gamma^2_{R_z}} \tag{18}$$

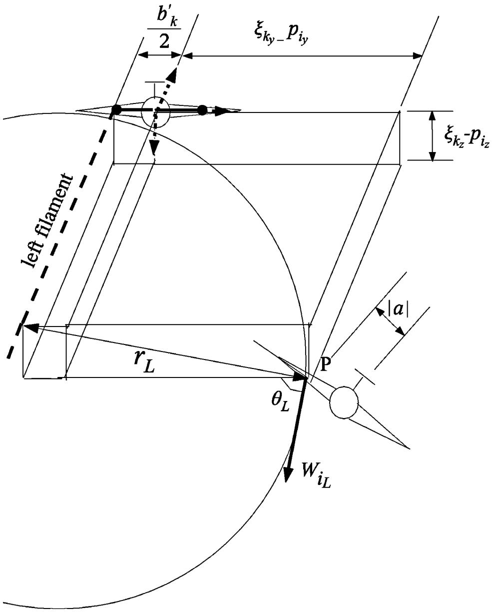

Fig. 6 Vortex model—a closer look.

Because the position vector $\underline{\boldsymbol{p}}_i$ is a function of the spanwise separation a from UAV$_i$'s wing-root quarter-chord, the vectors $\underline{\boldsymbol{R}}_{i_R}$ and radial distance r_R (and similarly $\underline{\boldsymbol{R}}_{i_L}$, r_L) are also functions of a.

A similar procedure is repeated to obtain the radial distance from point P to the left vortex filament also ($r_L = \sqrt{(\gamma_{L_y}^2 + \gamma_{L_z}^2})$.

Once the radial distances are obtained by the preceding step-by-step procedure, they are inserted into the equation from the vortex model to compute the induced velocity vector $\underline{\boldsymbol{W}}_{i_R}$ (and similarly $\underline{\boldsymbol{W}}_{i_L}$).

The angles between the induced tangential velocity vectors and the y axis of UAV$_k$'s wind frame are

$$\theta_R = \arctan\left(\gamma_{R_y}\big/\gamma_{R_z}\right), \qquad \theta_L = \arctan\left(\gamma_{L_y}\big/\gamma_{L_z}\right) \tag{19}$$

The component of the induced velocity vector $\underline{\boldsymbol{W}}_{i_R}$ acting in the upward direction (negative z direction) of UAV$_k$'s wind frame is

$$W_{\mathrm{UW}_{i_R}} = \left|\underline{\boldsymbol{W}}_{i_R}\right| \sin\theta_R \tag{20}$$

Though the subscript in Eq. (20) reads UW, which seems to be the abbreviation for upwash, the vector actually is along the z axis of UAV$_k$'s wind frame and not the body frame of UAV$_i$ as stated by the conventional definition of upwash. Similarly, $W_{\mathrm{UW}_{i_L}} = |\underline{\boldsymbol{W}}_{i_L}| \sin\theta_L$.

The net upward velocity in the wind frame of UAV$_k$, experienced by the point P, as a result of both the vortex filaments is given by

$$W_{\mathrm{UW}_{i_{\mathrm{net}}}} = W_{\mathrm{UW}_{i_R}} - W_{\mathrm{UW}_{i_L}} \tag{21}$$

where the minus sign is because the rotation of the left vortex filament is in the clockwise direction (see Fig. 6), while that of the right filament is in the counterclockwise direction.

Similarly, the components along the y axis of UAV$_k$'s wind frame as a result of the vectors $\underline{\boldsymbol{W}}_{i_R}$ and $\underline{\boldsymbol{W}}_{i_L}$ are calculated as $W_{\mathrm{SW}_{i_R}} = |\underline{\boldsymbol{W}}_{i_R}| \cos\theta_R$ and $W_{\mathrm{SW}_{i_L}} = |\underline{\boldsymbol{W}}_{i_L}| \cos\theta_L$. From Fig. 6, the net sideward velocity from both the vortex filaments is seen to be

$$W_{\mathrm{SW}_{i_{\mathrm{net}}}} = W_{\mathrm{SW}_{i_R}} - W_{\mathrm{SW}_{i_L}} \tag{22}$$

The component along the x axis of UAV$_k$'s wind frame is zero because the vortex-induced velocities are considered to be tangential to the hypothetical circle on the yz plane of UAV$_k$'s wind frame (Fig. 6).

Therefore, the vector of the net vortex-induced wind velocity acting on UAV$_i$ written in UAV$_k$'s wind frame is

$$\underline{\boldsymbol{W}}_{\mathrm{wk}} = [\underline{\hat{w}}_k]^T \begin{bmatrix} 0 \\ W_{\mathrm{SW}_{i_{\mathrm{net}}}} \\ -W_{\mathrm{UW}_{i_{\mathrm{net}}}} \end{bmatrix} \tag{23}$$

B. Effective Wind Components and Gradients on UAV$_i$

Vortex-induced velocites acting on an aircraft are highly nonuniform. Thus, standard aerodynamic force and moment equations, based on airspeed, angles of attack, and sideslip, and uniform wind components and gradients acting at the c.m. of the aircraft, cannot be used directly. That is the reason there have been a great number of research studies dealing with the estimation of induced forces and moments by trailing vortices.[6,11] To utilize the standard sets of equations of motion of an aircraft based on the motion of the c.m. of the aircraft relative to the surrounding air with uniform translational and rotational wind, an approximation technique for the wind flowfield induced by the trailing vortex around an encountering aircraft (UAV$_i$) is developed. This technique approximates the highly nonuniform flowfield by uniform wind components in and uniform wind gradients around the three-body axes of UAV$_i$. These three components and three gradients of wind are defined as the components and gradients of "effective wind at the center of mass" of UAV$_i$.

First, the wind field as a result of the trailing-edge vortices from UAV$_k$ is determined using a suitable vortex model in terms of the components of wind in three-body axes of UAV$_i$. Then, the components of wind, distributed nonuniformly over UAV$_i$, are used to compute the average values over intervals that are aligned with the body of UAV$_i$. When we take the average of a component of wind, we consider the variation of the component along the corresponding body axis of the aircraft. This is because only the wind acting on a specific part of the aircraft has an effect on the dynamics of the aircraft. The average values of the components of vortex flowfield over the corresponding intervals are then used to approximate the components and gradients of the effective wind at the center of mass of the aircraft. The components and gradients of the effective wind are used in the aircraft equations of motion that assume a uniform wind velocity and uniform wind gradient field.

The averaging technique implemented in our study to estimate the effective wind and wind gradient is as follows. First the vector of the net vortex-induced wind velocities written in the wind frame of UAV$_k$ (as obtained in the preceding section) needs to be transformed to the body frame of UAV$_i$ before averaging. This is because the wind velocity components (upwash, sidewash, and the frontwash) are defined in the body frame of the follower UAV$_i$. Furthermore, the estimation of the forces and moments created by the upwash, sidewash, the frontwash and the three components of air's local angular velocity becomes more direct in the body frame. Thus, the vector in Eq. (23) is written in UAV$_i$'s body frame as (refer to Fig. 2 for the sequence of rotation and the rotation matrices involved)

$$\begin{aligned} \underline{\boldsymbol{W}}_{\mathrm{Bi}} &= [\underline{\hat{B}}_i]^T \left(\boldsymbol{R}_{B_i\mathrm{VL}}\right)\left(\boldsymbol{R}^T_{B_k\mathrm{VL}}\right)\left(\boldsymbol{R}_{B_k w_k}\right) \begin{bmatrix} 0 \\ W_{\mathrm{SW}_{i_{\mathrm{net}}}} \\ -W_{\mathrm{UW}_{i_{\mathrm{net}}}} \end{bmatrix} \\ &= [\underline{\hat{B}}_i]^T \begin{bmatrix} W_x \\ W_y \\ W_z \end{bmatrix} \end{aligned} \tag{24}$$

Then, a series of averages of the components W_x, W_y, W_z are taken along the body parts of UAV$_i$ to approximate the effective translational and rotational wind velocity at its c.m. The point P is treated as the moving point to take the averages. In the body x direction, the average is taken by moving the point P over a length related to the entire length of the aircraft, from nose to the end of the fuselage. In the direction of the wing (which is the direction

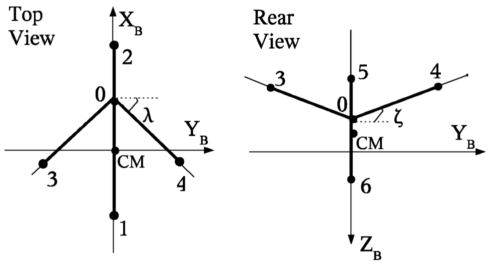

Fig. 7 Aircraft line diagram showing the integration limits along the body directions.

of the vector $\underline{\boldsymbol{a}}_i$), the point P is traversed from one wing tip to the other {which implies the value of a [Eq. (8)] is varied from $-b_i/2$ to $b_i/2$}. Along the body z axis, the averaging is done over a length that is of the order of the diameter of the fuselage of UAV$_i$ and perhaps the height of the vertical tail (as in the line diagram in Fig. 7).

For each of the velocity components W_x, W_y, and W_z, we take average along four lines, each along the two body directions that contribute to a moment about the c.m. of UAV$_i$. We then use these four averages to approximate the effective wind components ($W_{x_{\text{eff}}}$, $W_{y_{\text{eff}}}$, and $W_{z_{\text{eff}}}$) at the c.m. of UAV$_i$.

For example, to calculate the effective wind velocity in the body x direction of UAV$_i$ ($W_{x_{\text{eff}}}$), we calculate the average values along four lines, two on the body z axis of UAV$_i$-as seen in Fig. 7 one from point 5 to c.m. ($\tilde{W}_{x_{1z}}$) and the other from c.m. to point 6 ($\tilde{W}_{x_{2z}}$), and two on the UAV$_i$'s wing—one along the quarter-chord line on the left wing from point 3 to point 0 ($\tilde{W}_{x_{1y}}$), and the other along the quarter-chord line on the right wing from point 0 to point 4 ($\tilde{W}_{x_{2y}}$).

Then an approximation for the x component of the effective wind at c.m. is

$$W_{x_{\text{eff}}} = \left[\tilde{W}_{x_{1y}} + \tilde{W}_{x_{2y}} + \tilde{W}_{x_{1z}} + \tilde{W}_{x_{2z}}\right]\Big/4 \tag{25}$$

Next, the effective gradient of the x component of wind at c.m. about y and z directions, which are used in the rotational dynamics equations of UAV$_i$, are identified as $(\partial W_x/\partial y)_{\text{eff}}$ and $(\partial W_x/\partial z)_{\text{eff}}$. These gradients are estimated using the two averages along each of the two corresponding directions. Therefore,

$$\left(\frac{\partial W_x}{\partial y}\right)_{\text{eff}} = \frac{1}{b_i/2}\left[\tilde{W}_{x_{2y}} - \tilde{W}_{x_{1y}}\right] \tag{26}$$

$$\left(\frac{\partial W_x}{\partial z}\right)_{\text{eff}} = \frac{1}{D_{F_i}\big/2}\left[\tilde{W}_{x_{2z}} - \tilde{W}_{x_{1z}}\right] \tag{27}$$

Similarly, for the y and z components and gradients of the effective wind we get four average values each by integrating W_y from points 1 to 2 and 5 to 6 through c.m. and W_z from points 1 to 2 through c.m. and 3 to 4 through point 0, respectively. From these sets of four average values, the corresponding effective wind components ($W_{y_{\text{eff}}}$, $W_{z_{\text{eff}}}$) and gradients $(\partial W_y/\partial x, \partial W_y/\partial z, \partial W_z/\partial x, \partial W_z/\partial y)_{\text{eff}}$ are calculated using expressions similar to Eqs. (25–27).

In the preceding procedure, partial derivatives with respect to y $(\partial W_x/\partial y, \partial W_z/\partial y)_{\text{eff}}$ are approximated using the averages along the wing axis (i.e., a axis) and not body y axis. This approximation is done because, even if the wing axis does not coincide with the body y axis (because of nonzero sweep/dihedral angle of UAV$_i$), the effect of the vortex at any two corresponding points on the wing on the overall dynamics (specifically the rotational dynamics) of UAV$_i$ is parallel to its body y axis.

Once all of the three effective components of the induced wind velocity vector $\underline{\boldsymbol{W}}_i$ and the corresponding gradients are computed, they are introduced into the nonlinear aircraft equations (listed in Sec. VII), which include the components and the temporal variation of uniform wind in the body frame of the aircraft. Solving these nonlinear equations directly provides the effect of the vortex from UAV$_k$ on the dynamics of UAV$_i$.

IV. Vortex Models

A model for the velocity induced by a vortex is required to obtain the induced velocity vector acting at an arbitrary point P on UAV$_i$. We examined variations of the standard horseshoe vortex model with varying representations of the core. The classic Helmholtz horseshoe vortex model (HVM) is simple and yields good results for inviscid, incompressible flow conditions.[1,10,11] Following the notation introduced earlier and considering only the right vortex filament (a similar expression can be written for the left vortex filament), we get

$$W_{i_R} = \Gamma_k/(2\pi r_R) \tag{28}$$

where r_R is the radial distance from the point of interest P to the center of the vortex filament. The vortex strength is defined by

$$\Gamma_k = \tfrac{1}{2} C_{L_k} V_k \bar{c}_k \tag{29}$$

where C_{L_k} stands for the lift coefficient.

The singularity in the HVM model makes it unsuitable for the present work. The singularity can be overcome by including a term to account for a finite core radius. One nonsingular model, obtained from an exact solution to the unsteady Navier–Stokes equations, is given by Schlicting[12]

$$W_{i_R} = [\Gamma_k/(2\pi r_R)]\left[1 - e^{-(r_R^2/4\nu\tau)}\right] \tag{30}$$

Here, we approximate the vortex age by $\tau = (x_{B_k} - x_{B_i})/V_k$. This makes the vortex model dependent on the longitudinal separation between the two aircraft. Kurylowich[13] developed an alternate form of Eq. (30) by rewriting the exponent in terms of a core radius directly:

$$W_{i_R} = [\Gamma_k/(2\pi r_R)]\left[1 - e^{-1.26(r_R/r_c)^2}\right] \tag{31}$$

The core radius is related to the viscosity by the function

$$r_c = 2.24\sqrt{\nu\tau} \tag{32}$$

This results in a core that grows with time. Use of the actual fluid viscosity gives peak velocities that are far too large compared to published data. We varied the viscosity parameter and found that a value equal to 0.06 × Γ closely matched the velocity distribution given by Rossow and James.[14] For the aircraft to be analyzed in Sec. VI, this corresponds to a core radius of

$$r_c = 0.84\sqrt{\tau} \tag{33}$$

Results using this value for the core radius will be referred to hereafter as the modified HVM. Kurylowich developed an empirical expression for the core radius, which for the present case gives

$$r_c = 0.52\sqrt{\tau} \tag{34}$$

Results using this value for the core radius will be referred to as the Kurylowich model. A more recent representation of the velocity profile was developed by Burnham[1]:

$$W_{i_R} = (\Gamma_k/2\pi)\left[r_R\Big/\left(r_R^2 + r_c^2\right)\right] \tag{35}$$

Our application of the Burnham model uses the Kurylowich value for the core radius.

In Sec. VI, the basic HVM is used to analytically verify the induced rolling moment predicted by our averaging scheme with that using a theoretical method provided by Kurylowich. The other vortex models, in which the singularity in the vortex-induced velocity has been eliminated, are applied to the actual simulation used to calculate and compare the incremental force and moment coefficients.

V. Averaging Schemes

The general form of the various averaging schemes applied in our study to estimate the effective wind components and gradients is as follows: For each of the velocity components W_x, W_y, and W_z, we take averages along four lines, two each along the two body directions that contribute to a moment about the c.m. of the aircraft. We then use these four averages to approximate the effective wind components and gradients at the c.m. of the encountering aircraft.

As explained in Sec. III.B, to calculate the component of the effective wind velocity in the body x direction of the aircraft ($W_{x_{\text{eff}}}$), we estimate four average values: $\tilde{W}_{x_{1y}}$, $\tilde{W}_{x_{2y}}$, $\tilde{W}_{x_{1z}}$, and $\tilde{W}_{x_{2z}}$. In mathematical form, the equations for the four averages are given by

$$\tilde{W}_{x_{1y}} = \frac{1}{b/2}\int_{a=-b/2}^{0} f_{xy}(a) W_x \,\mathrm{d}a \tag{36}$$

$$\tilde{W}_{x_{2y}} = \frac{1}{b/2}\int_{a=0}^{b/2} f_{xy}(a) W_x \,\mathrm{d}a \tag{37}$$

$$\tilde{W}_{x_{1z}} = \frac{1}{D_F/2}\int_{z=-D_F/2}^{0} f_{xz}(z) W_x \,\mathrm{d}z \tag{38}$$

$$\tilde{W}_{x_{2z}} = \frac{1}{D_F/2}\int_{z=0}^{D_F/2} f_{xz}(z) W_x \,\mathrm{d}z \tag{39}$$

where the functions $f_{xy}(a)$ and $f_{xz}(z)$ are two nondimensional functions used for weighting the pointwise W_x velocities before integrating them. Corresponding functions for W_y are $f_{yz}(z)$, $f_{y1x}(x)$, $f_{y2x}(x)$, and those for W_z are $f_{z1x}(x)$, $f_{z2x}(x)$, and $f_{zy}(a)$.

The reason for breaking f_{yx} into two different weighting functions f_{y1x} and f_{y2x} (and similarly f_{zx} into f_{z1x}, f_{z2x}) is because of the geometry of the wind-tunnel test model that was used for the comparison analysis. Unlike the lateral and vertical directions along which the c.m. is located on the line of symmetry (in other words, the points {3, 4} and {5, 6} are symmetric about the c.m., in Fig. 7), the c.m. of the line diagram of the aircraft is offset from the geometric center in the longitudinal direction. Hence, to implement this geometric asymmetry in the simulation model the integration range in the longitudinal direction is also made asymmetric about the c.m. location, extending from $-L_F/4$ to 0 behind the c.m. and from 0 to $3L_F/4$ ahead of the c.m. As a result, two different weighting functions are used for averaging the pointwise velocities along the body x axis, one for the set of points behind the c.m. and the second for those ahead of the c.m.

Next, the effective wind component $W_{x_{\text{eff}}}$ and wind gradients $(\partial W_x/\partial y, \partial W_x/\partial z)_{\text{eff}}$ at the c.m. are approximated using equations similar to Eqs. (25–27).

Though the same symbols [such as $\tilde{W}_{x_{1y}}$, $\tilde{W}_{x_{2y}}$, $\tilde{W}_{x_{1z}}$, and $\tilde{W}_{x_{2z}}$ in Eqs. (25–27)] are used in the equations for both the effective wind component and the wind gradients, in the effective wind component calculation, only the basic unweighted averaging scheme (Sec. V.A) is used, whereas in the effective wind gradient calculation various (unweighted and weighted) averaging methods are used to make a comparison analysis. The reason for applying the weighted averages to calculate only the effective wind gradients and not the effective wind components is because, physically, it is known that the wind acting on the aircraft's body at points farther away from the c.m. would generate greater moment about the c.m. than those closer, owing to the difference in its "moment arm," while the point of action of the wind is immaterial in the calculation of the effective wind components.

Similarly, for the y and z components and gradients of the effective wind we get four average values each by integrating W_y from points (see Fig. 7) 1 to 2 and 5 to 6 through c.m. and W_z from points 1 to 2 through c.m. and 3 to 4 through point 0, respectively. From these sets of four average values, the corresponding effective wind components ($W_{y_{\text{eff}}}$, $W_{z_{\text{eff}}}$) and gradients $(\partial W_y/\partial x, \partial W_y/\partial z, \partial W_z/\partial x, \partial W_z/\partial y)_{\text{eff}}$ are calculated using expressions similar to Eqs. (25–27).

A. Basic Unweighted Averaging

In this scheme, the pointwise velocity components W_x, W_y, and W_z calculated along the body parts of the encountering aircraft are used directly for averaging without any weighting factor being applied to them. In other words, the weighting functions in Eqs. (36–39) are all unity.

B. Weighted Averaging

To improve on the basic weighted averaging scheme, several techniques were tried by including relative weights to the points falling within the range of integration to compute the effective wind gradients. These weighted averages were applied to calculate only the effective wind gradients. Thus, the effective wind components remain unaffected by the various weighted averaging schemes to be discussed in this section.

Among the many different possibilities of choosing the weighting functions like f_{xy} and f_{xz} in Eqs. (36–39), we list four schemes we used to test our model with.

1. Linear Weight Ranging from 0 to 1

According to this scheme,

$$\begin{aligned} f_{xy} &= \frac{|a\cos\zeta\cos\Lambda|}{b/2}, & f_{zy} &= \frac{|a\cos\zeta\cos\Lambda|}{b/2} \\ f_{xz} &= \frac{|z|}{D_F/2}, & f_{yz} &= \frac{|z|}{D_F/2} \\ f_{z1x} &= \frac{|x|}{L_F/4}, & f_{y1x} &= \frac{|x|}{L_F/4} \\ f_{z2x} &= \frac{|x|}{3L_F/4}, & f_{y2x} &= \frac{|x|}{3L_F/4} \end{aligned} \tag{40}$$

The motivation for this way of scaling the pointwise velocities is that physically the points farther away from the c.m. will have a greater influence on the effective gradients than those closer. It was found that using this scaling the effect of closer points were almost ignored, whereas the effect of the farthest point in each axial direction was maintained as before.

2. Linear Weight Ranging from 1 to 2

By this scheme,

$$\begin{aligned} f_{xy} &= 1 + \frac{|a\cos\zeta\cos\Lambda|}{b/2}, & f_{zy} &= 1 + \frac{|a\cos\zeta\cos\Lambda|}{b/2} \\ f_{xz} &= 1 + \frac{|z|}{D_F/2}, & f_{yz} &= 1 + \frac{|z|}{D_F/2} \\ f_{z1x} &= 1 + \frac{|x|}{L_F/4}, & f_{y1x} &= 1 + \frac{|x|}{L_F/4} \\ f_{z2x} &= 1 + \frac{|x|}{3L_F/4}, & f_{y2x} &= 1 + \frac{|x|}{3L_F/4} \end{aligned} \tag{41}$$

the effect of the closest point was maintained while that of the farthest point was made twice its original value.

3. Linear Weight Starting from 0

Among the two gradients $(\partial W_z/\partial y, \partial W_y/\partial z)_{\text{eff}}$ contributing to p_{eff}, the length of the aircraft body affected by W_z (length along the wing) is larger than the length of the aircraft body affected by W_y (length along the body z direction). Thus, the effect of W_z gradient on p_{eff} should be greater than that of W_y. To include this factor, in the next weighting scheme the pointwise displacements present in the weighting functions are scaled by the largest dimension involved in the computation of the two gradients contributing to each of the effective body angular velocities. For example, in the case of p_{eff} both the weighting functions f_{zy} and f_{yz} are scaled by $b/2$, which is the largest among the four lengths considered for the averages corresponding to p_{eff}. Extending the same idea to the other body angular velocities and hence to the other wind gradients, we get the weighting functions to be

$$\begin{aligned} f_{xy} &= \frac{|a\cos\zeta\cos\Lambda|}{3L_F/4}, & f_{zy} &= \frac{|a\cos\zeta\cos\Lambda|}{b/2} \\ f_{xz} &= \frac{|z|}{3L_F/4}, & f_{yz} &= \frac{|z|}{b/2} \\ f_{z1x} &= \frac{|x|}{3L_F/4}, & f_{y1x} &= \frac{|x|}{3L_F/4} \\ f_{z2x} &= \frac{|x|}{3L_F/4}, & f_{y2x} &= \frac{|x|}{3L_F/4} \end{aligned} \tag{42}$$

By this scheme, the weighting function would vary from 0 to 1 in the longer displacement direction, whereas in the other it would range from 0 to a number less than 1. Hence the name of this scheme.

4. *Linear Weight Starting from 1*

Applying the same argument as in Sec. II to the scheme in Sec. III, we get its new variation as

$$\begin{aligned} f_{xy} &= 1 + \frac{|a\cos\zeta\cos\Lambda|}{3L_F/4}, & f_{zy} &= 1 + \frac{|a\cos\zeta\cos\Lambda|}{b/2} \\ f_{xz} &= 1 + \frac{|z|}{3L_F/4}, & f_{yz} &= 1 + \frac{|z|}{b/2} \\ f_{z1x} &= 1 + \frac{|x|}{3L_F/4}, & f_{y1x} &= 1 + \frac{|x|}{3L_F/4} \\ f_{z2x} &= 1 + \frac{|x|}{3L_F/4}, & f_{y2x} &= 1 + \frac{|x|}{3L_F/4} \end{aligned} \tag{43}$$

As shown in Sec. VI, this weighting method produced the best results.

There are a multitude possibilities for developing more sophisticated schemes. For example, a function could be designed to show that for the calculation of p_{eff}, W_z acts over a larger area in the yz plane of the body axis (wing planform area) than W_y in the xz plane of the body axis (area of the fuselage in the side view of the aircraft), so that $(\partial W_z/\partial y)_{\text{eff}}$ and $(\partial W_y/\partial z)_{\text{eff}}$ could be weighted appropriately. In the present study, because the results with the relatively simpler techniques just discussed showed qualitatively and in many cases quantitatively sufficient matching, no attempt was taken to develop a more sophisticated weighted averaging scheme.

C. Number of Terms in p_{eff} and q_{eff}

In general form, the effective induced body angular rates are given by

$$p_{\text{eff}} = \left(\frac{\partial W_z}{\partial y}\right)_{\text{eff}} - \left(\frac{\partial W_y}{\partial z}\right)_{\text{eff}} \tag{44}$$

$$q_{\text{eff}} = \left(\frac{\partial W_x}{\partial z}\right)_{\text{eff}} - \left(\frac{\partial W_z}{\partial x}\right)_{\text{eff}} \tag{45}$$

$$r_{\text{eff}} = \left(\frac{\partial W_y}{\partial x}\right)_{\text{eff}} - \left(\frac{\partial W_x}{\partial y}\right)_{\text{eff}} \tag{46}$$

Of these three angular velocities, the lengths involved in the calculation of the two derivatives in Eq. (46) for r_{eff} are almost equal, whereas those in Eqs. (44) and (45) are significantly different for typical aircraft. For a configuration without a vertical tail, the dz terms are extremely small, and so it is reasonable to consider neglecting these entirely:

$$p_{\text{eff}} = \left(\frac{\partial W_z}{\partial y}\right)_{\text{eff}} \tag{47}$$

$$q_{\text{eff}} = -\left(\frac{\partial W_z}{\partial x}\right)_{\text{eff}} \tag{48}$$

This model for the wind-induced body rates very closely resembles the one presented by Etkin.[15] The effect of dropping these terms will be calculated in the next section.

VI. Vortex-Effect Model Comparison Analysis

This section will 1) compare the result from our method with a classical method as a sanity check and 2) compare our results with a set of wind-tunnel data obtained on two aircraft in formation.

A. Analytical Comparison

The induced rolling moment computed by our technique will be compared to the theoretical result given by Kurylowich[13] for the case of a vortex whose axis is parallel to the chord of a rectangular wing (Fig. 8).

1. *Kurylowich Method*

Using strip theory with the Helmholtz vortex model, the rolling moment induced by a vortex in the plane of an untapered wing, with the vortex core being outside the wing tip, is

$$\frac{-2\pi V b}{\Gamma C_{L_\alpha}} C_l = -1 + \frac{Y}{b} \ln \frac{2(Y/b)+1}{2(Y/b)-1} \tag{49}$$

If the vortex core is assumed to be one span to the right ($Y = b$) from the centerline of the encountering wing, then

$$C_l = \left(-\Gamma C_{L_\alpha}\big/2\pi V b\right)(-1 + \ln 3) \approx -0.0157\left(\Gamma C_{L_\alpha}\big/V b\right) \tag{50}$$

2. *Our Averaging Method*

Using the same Helmholtz profile,

$$W_z = \Gamma/2\pi(b-y) \tag{51}$$

because the radial distance between the point of interest and the vortex core is $b - y$ for the given relative separation between the encountering aircraft and the vortex filament. Here y denotes the instantaneous position of the point moved along the wing to

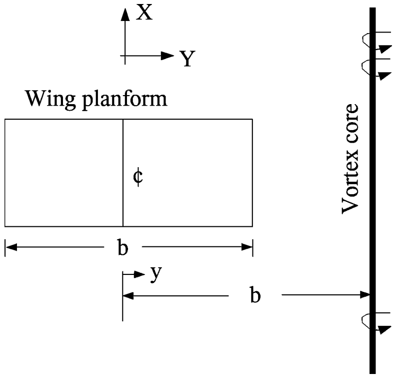

Fig. 8 Relative separation considered for analytical check.

compute the effective wind component and gradients (Fig. 8). Employing our averaging technique,

$$\begin{aligned}\tilde{W}_{z_y} &= \frac{1}{(b/2)}\int W_z\,\mathrm{d}y = \frac{1}{(b/2)}\int \frac{\Gamma}{2\pi(b-y)}\,\mathrm{d}y \\ &= \frac{-\Gamma}{\pi b}\ln[1-(y/b)] \end{aligned} \tag{52}$$

where the average is taken from $-(b/2)$ to 0 for the left wing and 0 to $b/2$ for the right wing, we get for the left wing

$$\tilde{W}_{z_{1y}} = (\Gamma/\pi b)(\ln 3 - \ln 2) \tag{53}$$

and for the right wing

$$\tilde{W}_{z_{2y}} = (\Gamma/\pi b)(\ln 2) \tag{54}$$

Thus, the effective roll gradient is

$$\begin{aligned}p_{\mathrm{eff}} &= \left(\frac{\partial W_z}{\partial y}\right)_{\mathrm{eff}} = \frac{1}{b/2}\left[\tilde{W}_{z_{2y}} - \tilde{W}_{z_{1y}}\right] \\ &= \frac{2\Gamma}{\pi b^2}(2\ln 2 - \ln 3)\end{aligned} \tag{55}$$

By strip theory,[16] rolling-moment coefficient for an untapered wing is

$$C_{l_p} = -C_{L_\alpha}\big/6 \tag{56}$$

So, the roll induced by our method will be

$$\begin{aligned}C_l &= C_{l_p}(p_{\mathrm{eff}}b/2V) = \left(-C_{L_\alpha}\big/6\right)(2\Gamma/\pi b^2)(2\ln 2 - \ln 3)(b/2V) \\ &= \left(-\Gamma C_{L_\alpha}\big/6\pi V b\right)(2\ln 2 - \ln 3) \approx -0.0153\left(\Gamma C_{L_\alpha}\big/Vb\right)\end{aligned} \tag{57}$$

From Eqs. (50) and (57), we can see that both of the methods give almost exactly the same result. Therefore, our method predicts the rolling moment quite accurately for a conventional aircraft with a rectangular planform wing.

B. Comparison to Wind-Tunnel Results

This section discusses the results of the comparison study conducted using our averaging method and a set of wind-tunnel measurements pertaining to the case of two aircraft flying in close formation.[17] For this case, the vortex-generating aircraft is referred to as the lead (or leader) aircraft, and the encountering aircraft is referred to as the trail (or follower) aircraft.

1. Representation of Wind-Tunnel Test Model

The aircraft model used for the wind-tunnel test[17] was a Lockheed tailless aircraft design consisting of a 65-deg delta wing with a sawtooth trailing edge with sweep angles of 25 deg. It is a single-engine design with two narrow inlets on the lower surface. For the test, the inlets were blocked, and both the lead and the trail aircraft were mounted at an 8-deg angle relative to the freestream. The trail aircraft had several bumps and exposed rods to accommodate internally actuated control surfaces.

In contrast to the untapered wing used for the analytical comparison, the wind-tunnel model used for data comparison is a delta-wing configuration varying trailing-edge sweep. To use our method, an effective quarter chord sweep angle needs to be defined. A change in sweepback angle of the aircraft results in a corresponding change in the radial distances to the vortex filaments and thus in the induced tangential velocities, which are used for the computation of the effective wind components and gradients. Hence, to approximate the 65-deg delta angle, a sweepback angle of 30 deg (which is close to the arithmetic average of 65-deg sweep at the leading edge and 0-deg effective sweep at the trailing edge) is included in the simulation model.

Next, in the computation of the incremental coefficients (Sec. II), the reference length for integration along the z direction is greatly reduced because the actual wind-tunnel test model was thin. Further, as explained in Sec. V, because the wind-tunnel model is a delta wing and its line diagram representation has a sweepback angle, we use an asymmetric integration region. (The integration length ahead of the c.m. is three times that behind.) These modifications help in finding a better match for yawing- and rolling-moment distributions.

2. Computation of the Incremental Force and Moment Coefficients

The novelty of our approach is that the induced forces and moments caused by the trailing vortex need not be computed directly in order to incorporate vortex effects on the dynamics of the encountering UAV. Instead, the effective wind components in and effective wind gradients around the body axes are directly used in the equations of motion and the aerodynamic buildup equations. However, because the wind-tunnel data are provided in terms of induced force and moment coefficients a similar approach is taken to obtain a comparative set of data. The aerodynamic buildup equations are assumed to be of the following form:

$$C_D = C_{D_0} + \frac{\partial C_D}{\partial \alpha^2}\alpha^2 \tag{58}$$

$$C_S = C_{S_0} + C_{S_\beta}\beta + C_{S_p}\left(\frac{pb}{2V}\right) + C_{S_r}\left(\frac{rb}{2V}\right) \tag{59}$$

$$C_L = C_{L_0} + C_{L_\alpha}\alpha + C_{L_q}\left(\frac{qc}{2V}\right) \tag{60}$$

$$\begin{aligned}C_l &= C_{l_0} + \left(C_{l_{\beta_0}} + \frac{\partial C_{l_\beta}}{\partial \alpha}\alpha\right)\beta + C_{l_p}\left(\frac{pb}{2V}\right) \\ &\quad + \left(C_{l_{r_0}} + \frac{\partial C_{l_r}}{\partial \alpha}\alpha\right)\left(\frac{rb}{2V}\right)\end{aligned} \tag{61}$$

$$C_m = C_{m_0} + C_{m_\alpha}\alpha + C_{m_q}\left(\frac{qc}{2V}\right) \tag{62}$$

$$C_n = C_{n_0} + C_{n_\beta}\beta + C_{n_p}\left(\frac{pb}{2V}\right) + C_{n_r}\left(\frac{rb}{2V}\right) \tag{63}$$

The values of the coefficients used are provided in the Appendix. In the preceding equations, the effective values of velocity V, angle of attack α, and the sideslip angle β are used for the calculations. The sideslip for the baseline case is zero, and so the effective β is solely a measure of the sideslip angle induced by the vortex field.

First, the effective velocity is determined using the relation

$$V = \boldsymbol{R}_{\mathrm{BI}}V_w + W_{\mathrm{eff}} \tag{64}$$

where $V_w = [V_{\mathrm{wt}}\ \ 0\ \ 0]^T$ is the velocity as a result of the wind-tunnel airspeed V_{wt} only (without the vortex effect) written in the wind frame of the trail aircraft and $W_{\mathrm{eff}} = [W_{x_{\mathrm{eff}}}\ \ W_{y_{\mathrm{eff}}}\ \ W_{z_{\mathrm{eff}}}]^T$ is the contribution from the vortex-induced effective wind components written in its body frame. For the wind-tunnel test condition, the wind frame of the trail aircraft is aligned with the inertial frame. However, because the test model is mounted with 8-deg pitch angle the body frame and the inertial frame are not aligned with each other. Therefore, we transform V_w from the wind frame to the body frame using the rotation matrix $\boldsymbol{R}_{\mathrm{BI}}$ before computing the effective velocity. Then, from the elements of the effective velocity vector the effective angles are derived as

$$\alpha = \mathrm{atan}\,(V_z/V_x) \quad \beta = a\sin\left(V_y\Big/\sqrt{V_x^2 + V_y^2 + V_z^2}\right) \tag{65}$$

where (V_x, V_y, V_z) are the components of the resultant velocity vector in the body frame of the trail aircraft. Figure 9 shows a

Table 1 Cases presented in comparison plots

Case no.	Vortex model	Weighting for effective wind component calculation	Weighting for effective wind gradient calculation	No. of terms in $p_{\text{eff}}, q_{\text{eff}}$
1	Modified HVM	No weighting	No weighting	2 terms
2	Modified HVM	No weighting	As in Sec. V.B.4	2 terms
3	Modified HVM	No weighting	No weighting	1 term
4	Modified HVM	No weighting	As in Sec. V.B.4	1 term
5	NASA Burnham	No weighting	As in Sec. V.B.4	1 term
6	Kurylowich	No weighting	As in Sec. V.B.4	1 term

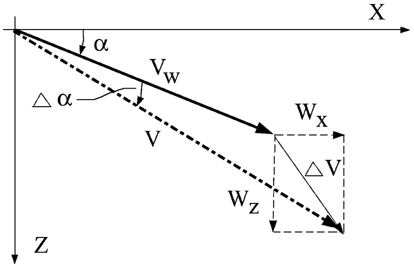

Fig. 9 Computation of effective angle of attack.

two-dimensional representation of this procedure for the case of α (XZ axes of the follower's body frame).

Also, the body angular velocities p, q, r are computed using the following relation:

$$\begin{bmatrix} p \\ q \\ r \end{bmatrix} = - \begin{bmatrix} p_{\text{eff}} \\ q_{\text{eff}} \\ r_{\text{eff}} \end{bmatrix} \tag{66}$$

where the induced body rates p_{eff}, q_{eff}, and r_{eff} are derived from the effective wind gradients (obtained as described in Sec. VI.B). The wind-tunnel test was a static test, so that the original body angular rates are considered to be zero; hence, the total angular velocities are just those induced by the vortex.

A series of computations were conducted that compared the incremental force and moment coefficients predicted by our model against the wind-tunnel measurements. During this comparison study, different vortex models, different averaging schemes, different weighting functions, and a different number of terms (partial derivatives) in p_{eff}, q_{eff} were applied in our vortex-effect modeling technique to find the best match between the computed forces and moments and the experimentally measured values. The region and limits of integration in the averaging process to estimate the effective wind components and effective wind gradients were also varied to help find a better match.

As a check of the internal coding of our model, we computed the force and moment coefficients on the trail aircraft for the case of no lead aircraft ahead of it. These results will be referred to as the baseline data. The longitudinal results matched exactly, as expected. The lateral-directional results did not match exactly, as our model predicts zero for the parameters at zero sideslip, whereas the wind-tunnel results showed small but nonzero values. These are inherent in every wind-tunnel test and arise from flow angularity, slight model asymmetries, etc. For the actual comparisons, we accounted for these discrepancies by using incremental force and moment coefficients instead of the absolute values. These were obtained by subtracting the baseline values from the data obtained with both aircraft in formation.

Initially, we introduced a lead aircraft whose position was fixed in space. The trail aircraft was separated by two spans ($2b$) in the longitudinal direction, one span in the lateral direction, and zero in the vertical direction. The pointwise velocity was computed by using one of the vortex models described in Sec. IV to evaluate the x, y, z components of the vortex-induced wind at a point that is moved along the trail aircraft's body x, z axes, and the wing axis. From the pointwise velocities, we estimated the effective wind components and the effective wind gradients acting on the trail aircraft using one of the averaging schemes discussed in Sec. V.

The undisturbed velocity of the lead and trail aircraft was considered to act along the inertial x direction (which is along the wind-tunnel test section horizontal). Hence, using the rotation matrix from the inertial frame to the body frame of the follower the undisturbed velocity components along the body axes of the trail aircraft are computed. The effective wind component vector was then added to the original velocity vector of the trail aircraft to obtain the resultant velocity vector. Using the components of this resultant velocity vector, the resultant angle of attack and sideslip angles were determined. These resultant angles and angular velocities (obtained from the effective gradients) were used to compute the absolute forces along and the absolute moments about all three body axes of the trail aircraft from Eqs. (58–63). Incremental force and moment coefficients were generated by calculating the difference between the coefficients corresponding to the baseline case and that with a lead aircraft ahead of the trail.

The vortex-induced effects were studied by comparing the incremental force and moment coefficients predicted by our code with those generated from the wind-tunnel measurements. The absolute forces and moments were also computed and plotted to compare directly with those measured in the wind tunnel. (These plots are not presented because of the similarity in the distribution of the absolute forces and moments with the corresponding incremental coefficients.)

3. *Test Cases*

Presenting the entire list of test cases is futile because of the many different combinations of vortex models, pointwise weighting, and expressions for p_{eff}, q_{eff}. Only the cases that showed the most promising results will be presented (Table 1). For the tailless aircraft of interest, lift and drag are the induced forces of primary interest, whereas the rolling and pitching moments are the important induced moments. Results for the side force and yawing moment were extremely small and will not be presented.

Based on the overall results obtained from the entire set of test cases, the modified HVM is observed to be the best vortex model. The weighting scheme given in Sec. V.B.4 together with Eqs. (46–48) proves to be the best method to compute the effective wind gradients and the induced body angular rates.

The objective of our vortex-effect modeling technique is only to develop an approximate model of aerodynamic coupling that is computationally efficient and can be included easily in the dynamic simulation of close proximity flight.[4,5] Hence a qualitative match with experimental results is considered to be sufficient, even if the accurate quantitative match as produced by some techniques involving discretization (such as vortex lattice[17]) is not obtained.

4. *Effect of Averaging Schemes*

The effect of the averaging method will now be shown using the vortex model from the modified HVM. These results are cases 1, 2, 3, and 4 (Table 1).

Figure 10 shows the effect of averaging scheme on the effective body angular velocities when the lateral separation between lead and trail aircraft is varied. The longitudinal and vertical spacing are maintained at $2b$ and 0, respectively. The pointwise weighting

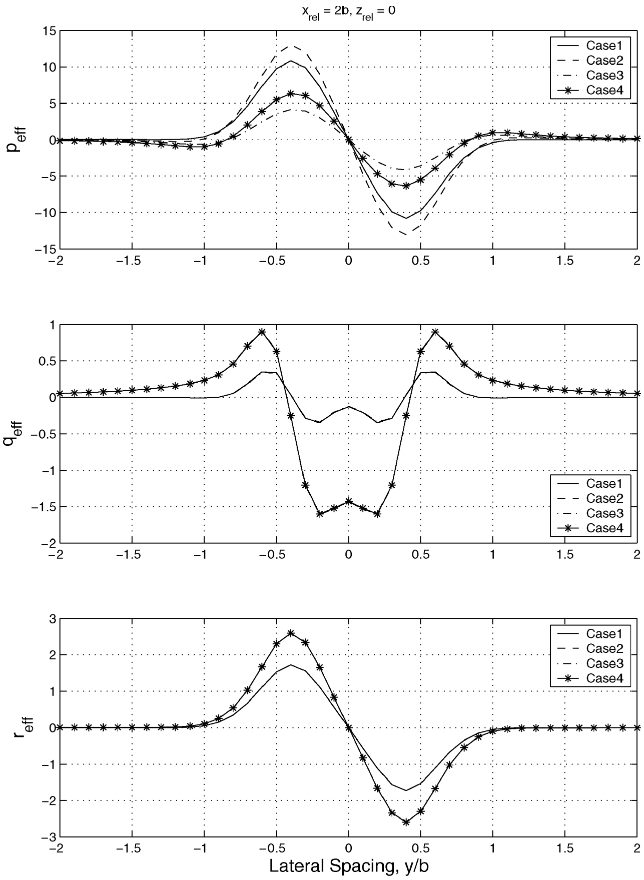

Fig. 10 Effect of averaging schemes on the effective body angular velocities.

as described in Sec. VI.B.4 (cases 2, 4) amplifies the values of the corresponding unweighted values (cases 1, 3). The effect of dropping a term in the equations for p_{eff} and q_{eff}, as described in Sec. VI.C is also shown. Recall that no term is dropped for r_{eff} between cases 1 and 3 and 2 and 4, so that only two out of four cases listed in the plot of r_{eff} are distinct. For p_{eff} and q_{eff}, the effect of dropping a term is more clearly visible in p_{eff} than in q_{eff}. For q_{eff}, the plots for cases 1 and 3 and 2 and 4 seem to coincide. This is because $(\partial W_x/\partial z)_{\mathrm{eff}}$, which is the term dropped in q_{eff} [unlike $(\partial W_y/\partial z)_{\mathrm{eff}}$, which is the term dropped in p_{eff}], is very small in magnitude for all lateral spacings.

The effect of averaging scheme on the wake-induced rolling moment is shown in Fig. 11. First, we note that case 1 also shows a zero crossing in the incremental rolling moment, but it is off the scale of the plot. As remarked in the discussion for Fig. 10, it can also be verified from Fig. 11 that the weighted averaging actually magnifies the unweighted curve on either side. As a result, the position of zero crossing seen in case 2 is better than that in case 1. The match gets very close to the experimental result when the additional terms in p_{eff} and q_{eff} are dropped and becomes almost a perfect match for case 4 with lateral spacing variation. For the vertical spacing variation, case 4 captures the trend and seems to have the closest match with the wind-tunnel measurement.

Figure 12 shows the effect of averaging schemes on the wake-induced pitching moment on the trail aircraft. As seen in the plots of p_{eff} in Fig. 10, cases 1 and 3 and 2 and 4 produce the same incremental pitching-moment distribution with variation in lateral spacing. A significant improvement in the magnitude of the pitching moment is caused as a result of the weighted averaging. The overall trend is in good agreement with the data (starting value has the same sign, sign change occurs at around the same lateral spacing, positive and negative slopes are also reasonably matched). Variation with vertical spacing also shows a nice trend match between the

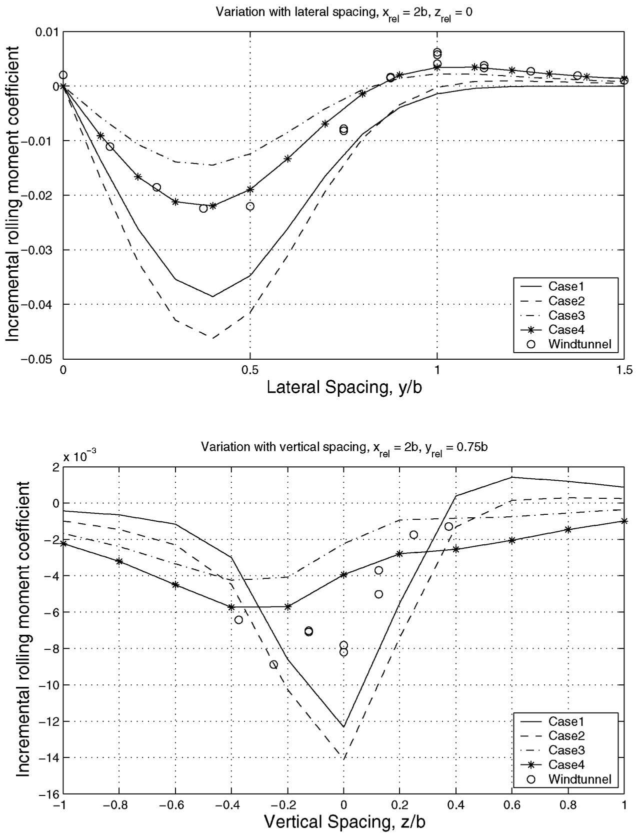

Fig. 11 Effect of averaging schemes on the wake-induced rolling moment.

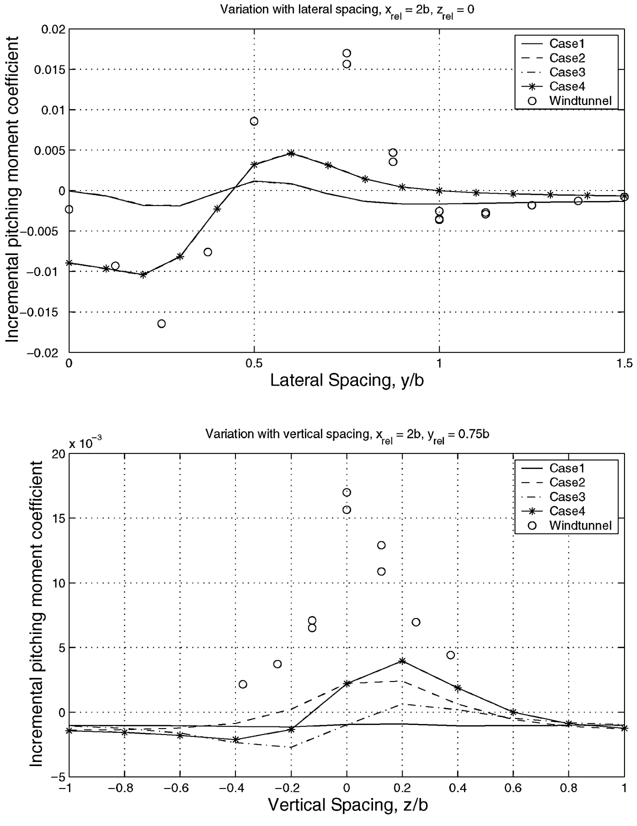

Fig. 12 Effect of averaging schemes on wake-induced pitching moment.

prediction by case 4 and the measured incremental pitching-moment coefficient, although the peak value is underpredicted. Although pointwise weighting causes the curve to rise as needed, dropping the additional term $[(\partial W_x/\partial z)_{\mathrm{eff}}]$ in q_{eff} introduces the sharp bends in the prediction (cases 3 and 4) that resemble the experimental data.

5. *Effect of Vortex Models*

Figure 13 shows the pointwise velocity distribution along the respective axes on the trail aircraft's body that are used to compute the effective wind and gradients. For this case, the separation of the trail aircraft relative to the leader is $[2b; b; 0]$, and both the leader and trail aircraft have an 8-deg pitch angle. The maximum W_z is experienced at the point directly behind the lead aircraft. At this point, the induced tangential velocities caused by both the right and left vortex filaments are aligned in the same (downwash) direction. A nonzero constant slope is observed in the variation of W_y when the point of interest is displaced along the body z axis. This is because the sideward components of the tangential velocity vector from the right and left vortex filaments do not cancel each other.

In Fig. 13, the lateral axis shown is not the body y axis but rather the axis along the wing (a axis) caused by the effect of wing sweep and dihedral angle. The differences observed in this figure between the three vortex models form the basis of the differences in the distributions of the effective wind components, gradients, and the induced forces and moments predicted for this specific relative separation between the lead and trail aircraft. Among the effective wind gradients contributing to the induced body angular rates, the most significant differences based on the pointwise velocity estimates between the various models are noticeable in $\partial W_z/\partial y$ for p_{eff}, $\partial W_x/\partial z$ for q_{eff}, and $\partial W_x/\partial y$ for r_{eff}, respectively. The presence of vortex decay in each model can be seen from the fact that the magnitudes of W_y and W_z tend asymptotically to zero along the body x axis.

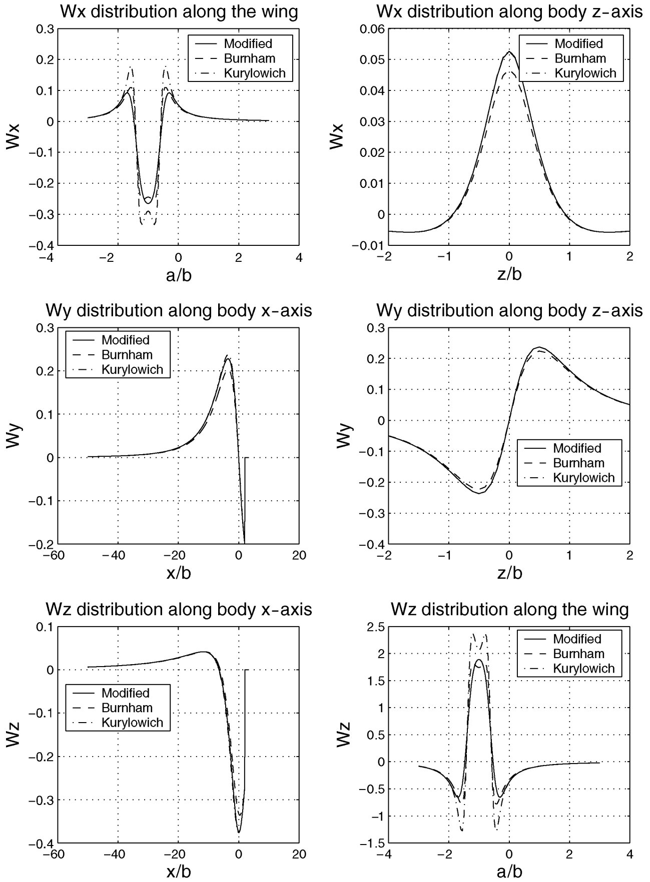

Fig. 13 Effect of vortex models on pointwise velocity distribution when $\xi_{\mathrm{rel}} = [2b; b; 0]$.

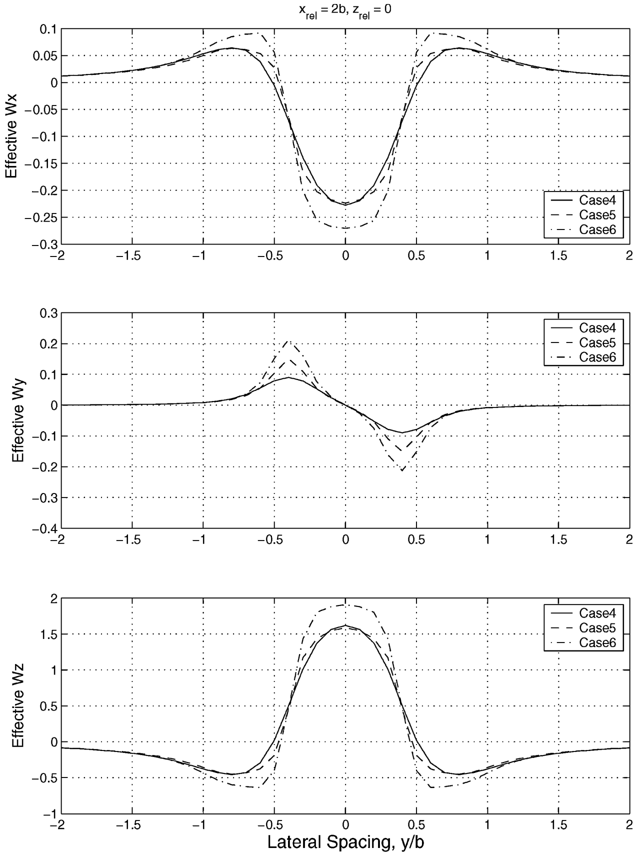

Fig. 14 Effect of vortex models on the effective wind components.

Given a pointwise velocity distribution, the effective wind components are computed using the unweighted averaging given in Sec. VI.A for various lateral separations (with $x_{\mathrm{rel}} = 2b$ and $z_{\mathrm{rel}} = 0$ kept unchanged) and plotted in Fig. 14. All of the vortex models produce the same qualitative distribution, with significant slope changes occuring near $y_{\mathrm{rel}} = 0$ and $y_{\mathrm{rel}} = 0.8b$.

Figure 15 compares the induced lift predicted by our method with the wind-tunnel measurements. Although modified HVM provides the best match in the lateral spacing of interest for formation flight ($y_{\mathrm{rel}} > 0.8b$), the Kurylowich model seems to exhibit a better slope at closer lateral proximities with the lead aircraft. Overall, predicted lift increments compare very well with the measured values for all of the vortex models. When vertical spacing is varied, the modified HVM and NASA Burnham models produce almost the same result and agree more closely with the data than the Kurylowich model. For the vertical spacing variation, $y_{\mathrm{rel}} = 0.75b$ was chosen as the lateral separation between the aircraft because it is close to the optimal spacing for formation flight [determined to be nearly $0.8b$ (Refs. 1 and 18)].

Figure 16 compares the predicted and measured rolling-moment increment, which is typically the largest vortex-induced moment and the one most critical to flight safety. The trend with lateral spacing is well predicted using all of the vortex models with the modified HVM providing the best match to the data. The zero crossing and peak magnitudes are very well predicted by this method. The trend with vertical spacing is a bit more erratic, but for the lateral location shown ($y/b = 0.75$) the induced moment is relatively small, especially compared with the case where the nose of the trail aircraft is aligned with the tip of the lead ($y/b = 0.5$).

Figure 17 compares the predicted and measured drag increment. The predicted increment is inviscid (induced drag only), whereas the wind-tunnel data include viscous effects. For reference, the total drag for the baseline case is 0.053 (data given in Appendix). The trend with lateral spacing is reasonably well predicted by all methods with the modified HVM method providing the closest match to the data. All of the methods show a zero crossing inboard of the actual

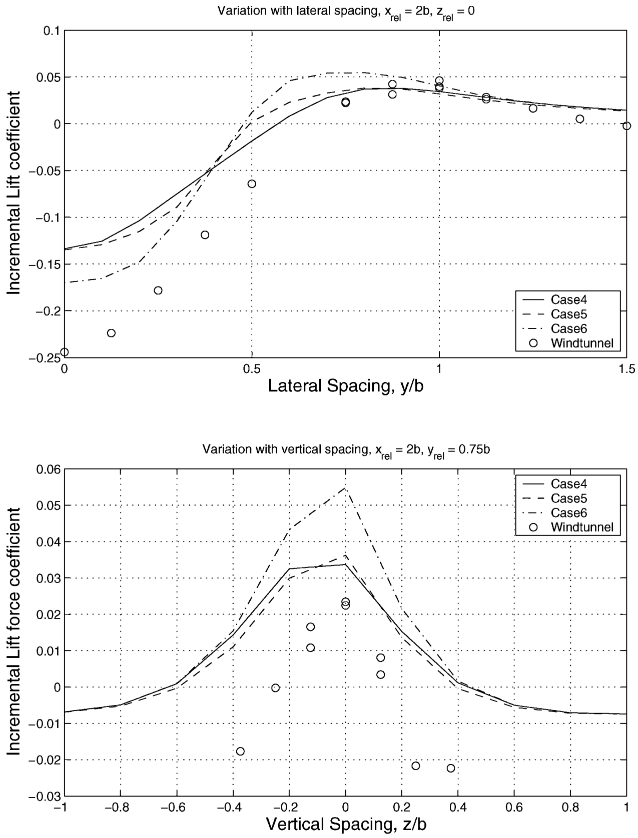

Fig. 15 Effect of vortex models on the wake-induced lift distribution.

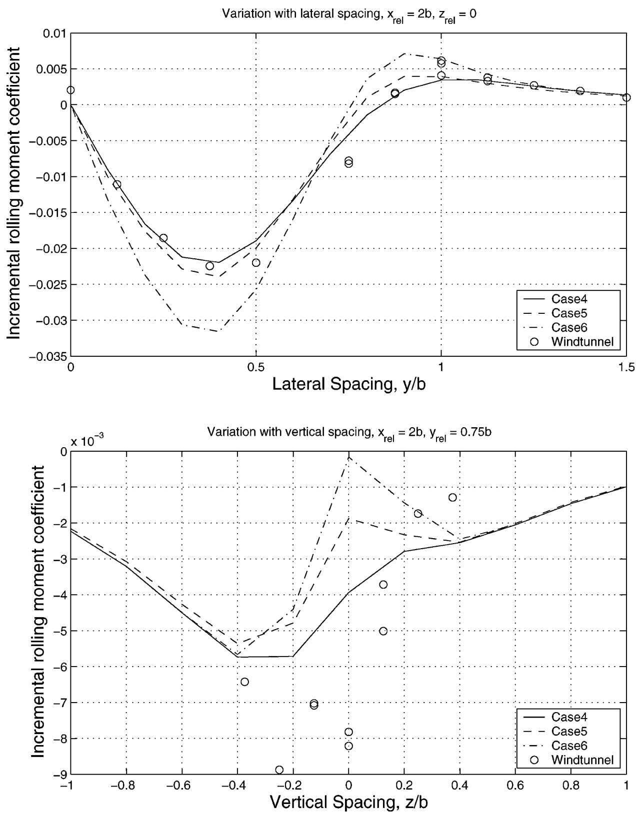

Fig. 16 Effect of vortex models on the wake-induced rolling-moment distribution.

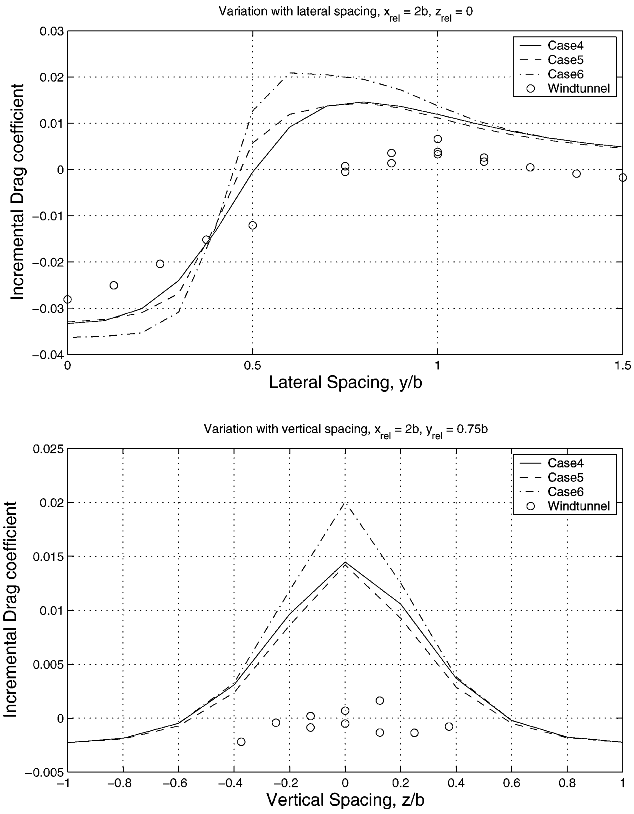

Fig. 17 Effect of vortex models on the wake-induced drag distribution.

value. The trend with vertical spacing is overpredicted, with an increase predicted for the in-plane case ($z/b = 0$) that the data do not show.

VII. Extension to Six-DOF Simulation

As stated earlier, the biggest advantage of our method is to approximate the nonuniform wind field as a result of the trailing vortex as uniform effective wind components and gradients, and then use them directly in the equations of motion of aircraft with wind terms. This way, the induced airspeed, angle of attack, and sideslip angle need not be computed, and furthermore there is no need to have additional force and moment terms for the induced forces and moments in the equations of motion.

Implementation of our method in the equations of motion of aircraft flying in close proximity is the subject of our other papers,[3–5,9] where we have developed six-DOF computer simulations and controllers for formation reconfiguration and aerial refueling. Here we briefly discuss how the proposed vortex modeling technique can be incorporated into a six-DOF dynamic simulation. The narrow focus is to explain the terms with the wind-related variables in the equations of motion. For the derivations and details of the dynamic equations, refer to the corresponding papers.[3–5,9]

The translational kinematics equation of a follower of an aircraft formation written in the virtual frame of the formation is given in matrix form as

$$\begin{bmatrix}\dot{x}_{B_i}\\ \dot{y}_{B_i}\\ \dot{z}_{B_i}\end{bmatrix} = \boldsymbol{R}^T_{B_i I}\boldsymbol{R}_{B_i w_i} V_i + \boldsymbol{R}^T_{B_i I} W_{\text{eff}} - \dot{\underline{\boldsymbol{r}}}_{\text{VL}} \tag{67}$$

where $\underline{\boldsymbol{r}}_{\text{VL}}$ is the position vector of the virtual leader frame with respect to an inertial frame. W_{eff} in the second term is the components of the wind in the body frame of the follower. In the derivation of this equation, it is assumed that the aircraft is exposed to a uniform wind and uniform wind gradient. Thus, using the method of this paper the effective wind components [as in Eq. (25)] are computed to approximate the vortex wind field as uniform wind and are directly used in the translational kinematics equations.

Similarly, the translational dynamics equation in matrix form is

$$\begin{bmatrix}\dot{V}_i\\ \dot{\beta}_i\\ \dot{\alpha}_i\end{bmatrix} = \mathcal{E}_i^{-1}\boldsymbol{S}\big(\omega_{B_i}\big)\boldsymbol{R}_{B_i w_i}V_i + \mathcal{E}_i^{-1}\boldsymbol{S}\big(\omega_{B_i}\big)W_{\text{eff}}$$

$$+ (1/m_i)\mathcal{E}_i^{-1}\big(\boldsymbol{R}_{B_i I}M_i + \boldsymbol{R}_{B_i w_i}A_i + P_i\big) - \mathcal{E}_i^{-1}\dot{W}_{\text{eff}} \tag{68}$$

where the airspeed V_i, sideslip angle β_i, and angle of attack α_i already include the vortex-induced effects. W_{eff} in the second term and $\dot{W}_{\text{eff}}$ in the last term are the effective wind and its derivative respectively, which are approximated using the averaging method explained in this paper.

The effects of the wind gradients in the rotational dynamics are seen explicitly in the moment coefficients. The buildup of the aerodynamic moment coefficients[3–5,9] is

$$C_{\mathcal{L}_i} = C_{\mathcal{L}_{0_i}} + C_{\mathcal{L}_{\delta_{a_i}}}\delta_{a\,i} + C_{\mathcal{L}_{\delta_{r_i}}}\delta_{r_i} + C_{\mathcal{L}_{\beta_i}}\beta_i$$

$$+ C_{\mathcal{L}_{p_i}}(b_i/2V_i)p_{i_{\text{rel}}} + C_{\mathcal{L}_{r_i}}(b_i/2V_i)r_{i_{\text{rel}}} \tag{69}$$

$$C_{\mathcal{M}_i} = C_{\mathcal{M}_{0_i}} + C_{\mathcal{M}_{\alpha_i}}\alpha_i + C_{\mathcal{M}_{\delta_{e_i}}}\delta_{e_i} + C_{\mathcal{M}_{q_i}}(\bar{c}_i/2V_i)q_{i_{\text{rel}}} \tag{70}$$

$$C_{\mathcal{N}_i} = C_{\mathcal{N}_{0_i}} + C_{\mathcal{N}_{\delta_{a_i}}}\delta_{a_i} + C_{\mathcal{N}_{\delta_{r_i}}}\delta_{r_i}$$

$$+ C_{\mathcal{N}_{\beta_i}}\beta_i + C_{\mathcal{N}_{p_i}}(b_i/2V_i)p_{i_{\text{rel}}} + C_{\mathcal{N}_{r_i}}(b_i/2V_i)r_{i_{\text{rel}}} \tag{71}$$

where $p_{i_{\text{rel}}}$, $q_{i_{\text{rel}}}$, $r_{i_{\text{rel}}}$ are the angular rotation of the aircraft relative to the air, not relative to the ground. Thus, the relative angular velocity components in the body frame are approximated by the effective wind gradients computed in Eqs. (46–48). The effects of the effective wind components in the rotational dynamics are implicit through the airspeed, sideslip angle, and angle-of-attack terms that the force equations and coefficients have. Similarly, the effects of the effective wind gradients in the translational dynamics are seen implicitly through $p_{i_{\text{rel}}}$, $q_{i_{\text{rel}}}$, and $r_{i_{\text{rel}}}$ the moment coefficients can have.

VIII. Conclusions

A novel method of incorporating the trailing vortex effect associated with aircraft flying in close proximity has been developed. The method computes effective wind and wind gradients on an aircraft as a result of trailing vortices from other aircraft. The winds are used to determine an effective velocity vector, angle of attack, and angle of sideslip for use directly in the wind-tunnel data comparison analysis. The wind gradients are used to determine an effective pitch, roll, and yaw rate on the trail aircraft. These rates are used in standard aerodynamic buildup equations for the moments. In the implementation of this method in the equations of motion including the wind terms, only the effective wind components and gradient are used. The effective velocity vector, angle of attack, and sideslip angle are the output of the solution of the differential equations.

Three models for estimating the tangential velocity caused by a vortex at a point on the trail aircraft were assessed. Five methods for averaging these velocities to define an effective wind gradient were studied. The number of terms retained in the calculation of the velocity gradients was also varied. The methods were assessed by comparing predicted force and moment increments with experimental data from a wind-tunnel test of two tailless aircraft in close proximity.

The vortex model that provided the best comparison to the measured data was a modified horseshoe vortex model with a finite core radius. The velocity averaging method that provided the best results used a linear weighted average with a weighting function that varied from one at the center of mass to a maximum of two at the configuration extremity (wing tip, nose, tail). For the velocity gradients, the best results were obtained when the effective roll rate included only the partial derivative of downwash in the lateral direction and the effective pitch rate, only the partial derivative of downwash in the longitudinal direction. The best combination of methods provided excellent matches to the wake-induced lift and rolling moment on the trail aircraft. The trends were well predicted for the drag and pitching moment although peak magnitudes were underpredicted.

The advantage of the proposed method is not to get a perfect match with wind-tunnel or flight data, but to have good enough match so that the standard aircraft equations of motion can be used directly without any modification required, but still include the effect of trailing vortex on the dynamics of the follower aircraft.

Appendix: Numerical Data

Note: The following data apply identically to each aircraft considered in the simulation. Although all of the angles are provided in degrees, in the simulation the values in radians are used.

Simulation Parameters

V_{wt}: 19.8171 m/s

Formation flight altitude (for air density calculation): sea level

Aircraft Parameters

$\mathcal{S}$: 0.4448 m^2
$\bar{c}$: 0.6744 m
b: 0.8796 m
D_F: 0.12 m
L_F: 1 m
x_0 : 0 m
z_0: 0 m
ζ: 0 deg
Λ: 30 deg

Aerodynamic coefficients: $C_{L_0} = 0.062369$; $C_{L_\alpha} = 0.0365$; $C_{L_q} = 0.0267$; $C_{D_0} = 0.013091$; $\partial C_D/\partial\alpha^2 = 0.0006289$; $C_{S_0} = 0$; $C_{S_\beta} = -0.000545$; $C_{S_p} = 0.000488$; $C_{S_r} = 0.000767$; $C_{l_0} = 0$; $C_{l_{\beta_0}} = 0.000409$; $\partial C_{l_\beta}/\partial\alpha = -0.0002$; $C_{l_p} = -0.002844$; $C_{l_{r_0}} = 0$; $\partial C_{l_r}/\partial\alpha = 0.0000524$; $C_{m_0} = -0.003167$; $C_{m_\alpha} = -0.000424$; $C_{m_q} = -0.007$; $C_{n_0} = 0$; $C_{n_\beta} = -0.0003615$; $C_{n_p} = -0.000401$; $C_{n_r} = -0.000157$

Baseline Condition

$\beta = 0$; $p = 0$; $q = 0$; $r = 0$

References

[1] Blake, W., and Multhopp, D., "Design, Performance and Modeling Considerations for Close Formation Flight," *Proceedings of the 1998 AIAA GNC Conference*, AIAA, Reston, VA, 1998, pp. 476–486.

[2] Bloy, A. W., and Khan, M. M., "Modeling of the Receiver Aircraft in Air-to-Air Refueling," *Journal of Aircraft*, Vol. 38, No. 2, 2001, pp. 393–396.

[3] Venkataramanan, S., and Dogan, A., "Dynamic Effects of Trailing Vortex with Turbulence & Time-Varying Inertia in Aerial Refueling," *Proceedings of the AIAA AFM Conference*, AIAA, Reston, VA, 2004.

[4] Venkataramanan, S., and Dogan, A., "Nonlinear Control for Reconfiguration of UAV Formation," *Proceedings of the AIAA GNC Conference*, AIAA, Reston, VA, 2003.

[5] Venkataramanan, S., "Dynamics and Control of Multiple UAVs Flying in Close Proximity," M.S. Thesis, Dept. of Mechanical and Aerospace Engineering, Univ. of Texas, Arlington, TX, Aug. 2004.

[6] Pachter, M., D'Azzo, J. J., and Proud, A. W., "Tight Formation Flight Control," *Journal of Guidance, Control, and Dynamics*, Vol. 24, No. 2, 2001, pp. 246–254.

[7] Jewell, W., and Stapleford, R., "Mathematical Models used to Simulate Aircraft Encounters with Wake Vortices," System Technology, Inc., TR 1035-4, FAA Rept., DOT-FA73WA-3276-1, Aug. 1975, pp. 38–57.

[8] Pan, H., and Kapila, V., "Adaptive Nonlinear Control for Spacecraft Formation Flying with Coupled Translational and Attitude Dynamics," *Proceedings of the 40th IEEE Conference on Decision and Control*, Vol. 3, IEEE, Arlington, VA, 2001, pp. 2057–2062.

[9] Venkataramanan, S., and Dogan, A., "A Multi-UAV Simulation for Formation Reconfiguration," *Proceedings of the AIAA MST Conference*, AIAA, Reston, VA, 2004.

[10] Houghton, E., and Brock, A., *Aerodynamics for Engineering Students*, EdwardArnold, Ltd., London, 1970.

[11] Johnson, W. A., Tepert, G. L., and Rediess, H. A., "Study of Control System Effectiveness in Alleviating Vortex Wake Upsets," *Journal of Aircraft*, Vol. 11, No. 3, 1974, pp. 148–154.

[12] Schlicting, H., *Boundary Layer Theory*, McGraw–Hill, New York, 1979.

[13] Kurylowich, G., "A Method for Assessing the Impact of Wake Vortices on USAF Operations," Air Force Flight Dynamics Lab., Technical Rept. 79-3060, Wright-Patterson AFB, OH, July 1979.

[14] Rossow, V., and James, K., "Overview of Wake-Vortex Hazards During Cruise," *Journal of Aircraft*, Vol. 37, No. 6, 2000, pp. 960–975.

[15] Etkin, B., "Turbulent Wind and Its Effect on Flight," *Journal of Aircraft*, Vol. 18, No. 5, 1981, pp. 327–345.

[16] Seckel, E., *Stability and Control of Airplanes and Helicopters*, Academic Press, New York, 1964, p. 231.

[17] Blake, W., and Gingras, D., "Comparison of Predicted and Measured Formation Flight Interference Effects," *Proceedings of the 2001 AIAA AFM Conference*, AIAA, Reston, VA, 2001, pp. 1–12.

[18] Jake, V., Ray, R., Ennix, K., and Walsh, K., "F/A-18 Performance Beneffts Measured During the Autonomous Formation Flight Project," NASA/TM-2002-210732, Sept. 2003.